

Article

Refocusing of Moving Targets in SAR Images via Parametric Sparse Representation

Yichang Chen ^{1,2} , Gang Li ^{2,*}, Qun Zhang ^{1,3} and Jinping Sun ⁴

¹ Institute of Information and Navigation, Air Force Engineering University, Xi'an 710077, China; cyc_2007@163.com (Y.C.); zhangqunnus@gmail.com (Q.Z.)

² Department of Electronic Engineering, Tsinghua University, Beijing 100084, China

³ Key Laboratory for Information Science of Electromagnetic Wave (Ministry of Education), Fudan University, Shanghai 200433, China

⁴ School of Electronic and Information Engineering, Beijing University of Aeronautics and Astronautics, Beijing 100191, China; sunjinpings@buaa.edu.cn

* Correspondence: gangli@tsinghua.edu.cn; Tel.: +86-10-6279-4095

Academic Editors: Xiaofeng Yang, Xiaofeng Li, Ferdinando Nunziata and Alexis Mouche

Received: 12 June 2017; Accepted: 31 July 2017; Published: 2 August 2017

Abstract: In this paper, a parametric sparse representation (PSR) method is proposed for refocusing of moving targets in synthetic aperture radar (SAR) images. In regular SAR images, moving targets are defocused due to unknown motion parameters. Refocusing of moving targets requires accurate phase compensation of echo data. In the proposed method, the region of interest (ROI) data containing the moving targets are extracted from the complex SAR image and represented in a sparse fashion through a parametric transform, which is related to the phase compensation parameter. By updating the reflectivities of moving target scatterers and the parametric transform in an iterative fashion, the phase compensation parameter can be accurately estimated and the SAR images of moving targets can be refocused well. The proposed method directly operates on small-size defocused ROI data, which helps to reduce the computational burden and suppress the clutter. Compared to other existing ROI-based methods, the proposed method can suppress asymmetric side-lobes and improve the image quality. Both simulated data and real SAR data collected by GF-3 satellite are used to validate the effectiveness of the proposed method.

Keywords: moving target imaging; parametric sparse representation (PSR); region of interest (ROI); synthetic aperture radar (SAR)

1. Introduction

Moving target imaging is an important task of synthetic aperture radar (SAR) [1–6]. Since SAR imaging algorithms were originally designed for stationary targets, the main challenge for SAR imaging of moving targets is to compensate the phase error caused by non-cooperative motion of targets. It is well known that the Doppler frequency shift caused by target movement results in the imaging position offset along the azimuth direction. Further, the change of the azimuth frequency modulation rate, which is related to the acceleration in range and the velocity in azimuth of the target, introduces defocus of moving targets in regular SAR images [7]. From the viewpoint of process flow, the existing methods of SAR moving target imaging can be generally divided into two types. (1) Methods based on the raw radar data [8–12]. These methods deal with the entire echo data reflected from both stationary background and moving targets. In fact, only a small part of the entire data is related to the moving targets, and therefore, processing on entire data will induce a large amount of clutter. The displaced phase center antenna (DPCA) and along track interferometry (ATI) can effectively suppress the clutter [13,14], which requires multiple channels and therefore is not suitable

for single-channel SAR systems. (2) Methods based on the region of interest (ROI) data [15–17]. This type of methods can effectively remove clutter and easily detect moving targets. Since only a small image contacting the ROI data is extracted from regular SAR imaging result, the amount of data to be processed is significantly reduced. Zhang et al. [16] proposed a high-resolution SAR imaging method of ground moving targets with defocused ROI data. The authors derive an exact analytic expression of the ROI data without approximation of the slant range. Ref. [16] assumed that the phase error arises from the unknown azimuth and range velocities in a specific model. Then, the azimuth and range equivalent velocities are estimated by a 2-D search, such that the maximum contrast of moving target image is reached. The image of target is obtained by Stolt interpolation with each pair of equivalent velocity parameters. However, the equivalent velocity cannot reflect the actual motion parameters of target in acceleration state, which results in the difficulty of determining the search interval of equivalent velocities. Even if the accurate equivalent velocities are estimated, the model mismatch problem would introduce high asymmetric side-lobes in the imaging result when the target is in an acceleration state.

Since the radar echo reflected from man-made moving targets are usually stronger than the background, in recent years, many sparsity-aware methods have been applied to SAR moving target parameter estimation and imaging [18–25]. Ref. [23,25] summarize the latest application of sparse processing in SAR systems. An approach to motion parameter estimation with low pulse repetition frequency based on compressed sensing (CS) theory is proposed in [19]. Ref. [20] also proposes a method for motion parameter estimation of moving target based on the raw radar data. However, complicated clutter suppression is required before motion parameter estimation. Ref. [21] presents a method for imaging of moving targets with multi-static SAR using an overcomplete dictionary. In Ref. [22], the authors divide a phase error into three subcategories and correct them by using a nonquadratic regularization approach. However, due to the heavy computational burden, this method may not be suitable for these targets occupying a large number of resolution cells. Onhon et al. utilize the sparsity-driven autofocus framework to solve the problem of moving target imaging in [18], where the phase error induced by target movement is corrected by the non-quadratic regularization approach. However, this method ignores the relationship between the phase error and the motion parameters. It needs to independently estimate the phase error of each sample data, thus increasing the unnecessary computational burden.

In this paper, we propose a parametric sparse representation method for SAR imaging of moving targets with ROI data. The parametric sparse representation technique has been utilized to ISAR imaging of rotating targets [26–28], SAR motion compensation [29], and moving target motion parameters estimation [12]. Differing from the previous work where the process flow starts from entire raw data, the proposed method in this paper is based on ROI data. Firstly, the complex image in ROI that contains the defocused moving target is extracted from the regular SAR image. Then, the principal components of the ROI data, which correspond to the dominant scatterers of a moving target, are represented by a parametric transform that is uniquely determined by a phase compensation parameter. By updating the reflectivities of the target and the parametric transform in an iterative fashion, the phase compensation parameter can be accurately estimated and the focused image of moving target can be obtained when the iterative process converges. Differing from the method in [16], which realizes the phase compensation by searching 2-D equivalent velocities of moving targets, in this paper, the phase compensation is achieved by estimating the phase compensation parameter in an iterative fashion. Experimental results based on both simulated and space-borne SAR data demonstrate that the proposed method outperforms the method in [16] in terms of the imaging quality of moving targets. Simulations also show that, compared to the method in [16], the proposed algorithm in this paper has a higher tolerance for model mismatch problem and is capable of providing satisfactory refocused image even when the target is moving in acceleration state.

The rest of this paper is organized as follows. The SAR signal model is reviewed in Section 2. The proposed method for moving target imaging is formulated in Section 3. The performance of the

proposed method is evaluated, with both simulated and measured data, in Section 4. Conclusions are presented in Section 5.

2. Signal Model

The geometry relationship between the platform and a moving target for side-looking SAR is shown in Figure 1. The horizontal axis denotes the azimuth direction, and the vertical axis denotes the slant-range direction. Assume that the SAR platform flies straight at a speed of V along the x -axis, and the velocities of a moving target in azimuth and range are v_x and v_r , respectively.

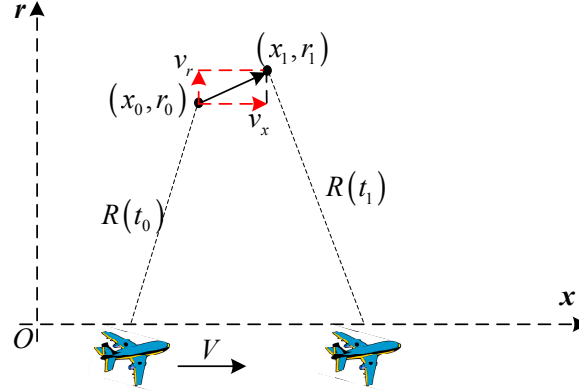


Figure 1. Geometry of synthetic aperture radar (SAR) imaging of a moving target.

The slow time is denoted as $t_s = nT$ with an integer n , and T is the pulse repetition time. Thus, the radar antenna phase center (APC) position at t_s is $(Vt_s, 0)$, and the position of the moving target is $(x_0 + v_x t_s, r_0 + v_r t_s)$, where (x_0, r_0) is the initial position when $t_s = 0$. The instantaneous distance between the moving target and the radar can be expressed as

$$R(t_s) = \sqrt{(Vt_s - x_0 - v_x t_s)^2 + (r_0 + v_r t_s)^2} \quad (1)$$

Suppose that the radar transmits a linear frequency-modulated (LFM) signal as

$$s(t, t_s) = \text{rect}(t/T_p) \cdot \exp(j2\pi f_c t + j\pi\gamma t^2), \quad (2)$$

where t is the fast time, T_p is the pulse width, $\text{rect}(\cdot)$ denotes the rectangular function, f_c is the carrier frequency, and γ is the chirp rate. The baseband echo of the moving target can be expressed as

$$s_r(t, t_s) = \sigma \cdot \text{rect}\left(\frac{t - 2R(t_s)/c}{T_p}\right) \cdot \text{rect}\left(\frac{t_s}{T_a}\right) \cdot \exp(-j4\pi f_c R(t_s)/c + j\pi\gamma(t - 2R(t_s)/c)^2), \quad (3)$$

where T_a is the synthetic aperture time, and the target scattering coefficient σ is assumed to be constant during the observation time interval. By taking the two-dimensional Fourier transform, the signal of the moving target in 2-D frequency domain can be expressed as

$$S_r(f_r, f_a) = \sigma \cdot W_r(f_r) \cdot W_a(f_a) \cdot \exp\left\{j \cdot \left[-2\pi f_a \frac{\delta}{v_e^2} - \pi \frac{f_r^2}{\gamma} - \frac{4\pi[x_0 v_r + r_0(V - v_x)]}{c v_e} \sqrt{(f_c + f_r)^2 - \frac{c^2 f_a^2}{4v_e^2}} \right] \right\}, \quad (4)$$

where f_r and f_a are the range and azimuth frequencies, respectively, $W_r(f_r)$ and $W_a(f_r)$ are the range and azimuth envelope function, respectively, $\delta = x_0(V - v_x) - r_0 v_r$ and $v_e = \sqrt{(V - v_x)^2 + v_r^2}$. After conventional matched filtering and Stolt interpolation, (4) becomes [16]

$$S_{r_Stolt}(f_r, f_a) = \sigma \cdot W_r(f_r) \cdot W_a(f_a) \cdot \exp \left\{ j \cdot \left[-2\pi f_a \frac{\delta}{v_e^2} - \frac{4\pi[x_0 v_r + r_0(V - v_x)]}{c v_e} \sqrt{(f_c + f_r)^2 + \frac{c^2 f_a^2}{4} \left(\frac{1}{V^2} - \frac{1}{v_e^2} \right)} \right] \right\}. \quad (5)$$

It can be seen from (5) that the high-order residual items still exist after the conventional SAR imaging processing, which means that the image of the moving target is defocused. To achieve a refocused image of moving target, it is necessary to compensate the residual phase items. The filter for residual phase compensation can be constructed as [16]

$$H_1(f_r, f_a) = \exp \left\{ j \cdot \left[\frac{4\pi R_{ref}}{c} \sqrt{(f_c + f_r)^2 + \frac{c^2 f_a^2}{4} \left(\frac{1}{V^2} - \alpha \right)} - \frac{4\pi R_{ref}}{c} (f_c + f_r) \right] \right\}, \quad (6)$$

where R_{ref} is the reference distance, and α is the phase compensation parameter, which is the parameter to be estimated in this paper. The phase compensation parameter is related to the motion parameters of target, and it can be expressed as $\alpha = 1 / \left[(V - v_x)^2 + v_r^2 \right]$ when the target is in uniform motion state. The phase compensation parameter becomes $\alpha = 1 / V^2$ when the target is stationary. This results in $H_1(f_r, f_a) = 1$ in (6), which means that no phase compensation is required for the data reflected from stationary targets. In the proposed method, we can initialize the phase compensation parameter as $1 / V^2$. By taking the two-dimensional inverse Fourier transform in (5), we can obtain the regular SAR complex image of observed scene, in which the sub-image that containing moving target is the so-called ROI data. The extracted ROI sub-image from the focused stationary background can be expressed as

$$s_{r_ROI}(\bar{t}, \bar{t}_s) = \sigma \cdot W_r \left(\bar{t} - \frac{2R_{ROI}(\bar{t}_s)}{c} \right) \cdot W_a \left(\bar{t}_s - \frac{\delta}{v_e^2} \right) \cdot \exp \left(-j \frac{4\pi}{\lambda} R_{ROI}(\bar{t}_s) \right), \quad (7)$$

where \bar{t} and \bar{t}_s denote the sampling index of ROI data in range and azimuth time domain, respectively, and

$$R_{ROI}(\bar{t}_s) = \sqrt{\left(\frac{x_0 v_r + r_0(V - v_x)}{v_e} \right)^2 - \left(\bar{t}_s - \frac{\delta}{v_e^2} \right)^2 \cdot \left(\frac{1}{V^2} - \frac{1}{v_e^2} \right)}, \quad (8)$$

In the next section, we will describe how to estimate the phase compensation parameter and refocus target image with the ROI data.

3. Parametric Sparse Representation Method for Moving Target Imaging

In this section, we formulate the parametric sparse representation method for imaging of moving targets. We denote the original image size as $N_r \times N_a$, and the ROI data size as $n_r \times n_a$. Note that the data size is significantly reduced, but the signal bandwidth of moving target remains unchanged. We define the range and azimuth frequency of ROI data as \bar{f}_r and \bar{f}_a , respectively. By taking two-dimensional Fourier transform in Equation (7), the ROI data in 2-D frequency domain can be expressed as

$$S_{r_ROI}(\bar{f}_r, \bar{f}_a) = \sigma \cdot W_r(\bar{f}_r) \cdot W_a(\bar{f}_a) \cdot \exp \left\{ j \cdot \left[-2\pi \bar{f}_a \frac{\delta}{v_e^2} - \frac{4\pi[x_0 v_r + r_0(V - v_x)]}{c v_e} \sqrt{(f_c + \bar{f}_r)^2 + \frac{c^2 \bar{f}_a^2}{4} \left(\frac{1}{V^2} - \frac{1}{v_e^2} \right)} \right] \right\}. \quad (9)$$

The phase compensation filter of ROI data can be rewritten as

$$H_{2(\alpha)}(\bar{f}_r, \bar{f}_a) = \exp \left\{ j \cdot \left[\frac{4\pi R_{ref}}{c} \sqrt{(f_c + \bar{f}_r)^2 + \frac{c^2 \bar{f}_a^2}{4} \left(\frac{1}{V^2} - \alpha \right)} - \frac{4\pi R_{ref}}{c} (f_c + \bar{f}_r) \right] \right\}. \quad (10)$$

The refocused image of the moving target can be obtained through a refocusing transform $\Gamma(\cdot)$:

$$\Theta = \Gamma(s_{r_ROI}) = \mathbf{\Psi}_r^{-1} \cdot \left[(\mathbf{\Psi}_r \cdot s_{r_ROI} \cdot \mathbf{\Psi}_a) \circ H_{2(\alpha)} \right] \cdot \mathbf{\Psi}_a^{-1}, \quad (11)$$

where Θ is the refocusing result of moving target, $\mathbf{\Psi}$ and $\mathbf{\Psi}^{-1}$ are the Fourier matrix and the inverse Fourier matrix, respectively. The subscripts r and a denote the range direction and azimuth direction, respectively, and \circ denotes Hadamard product. As shown in Equation (11), through a series of matrix operations, the refocusing transform $\Gamma(\cdot)$ can achieve the conversion from the defocused ROI data to the refocusing result of moving target. It is obvious that the image quality of Θ depends on the phase compensation parameter α , i.e., different phase compensation parameter produces different filter function $H_{2(\alpha)}$ and, therefore, different refocusing result Θ . Thus, Θ can be regarded as a function of α and denoted by $\Theta_{(\alpha)}$. With a wrong value of α , the refocusing transform $\Gamma(s_{r_ROI})$ will induce the high-order phase error in azimuth and range, and thus a blurred image is most likely obtained. With accurate estimate of α , the phase error of the ROI data can be well compensated, and accordingly, a well-focused moving target image will be obtained. From the above consideration, refocusing of the moving target can be carried out in an iterative fashion, i.e., the sparse imaging result Θ and the phase compensation parameter α are iteratively updated.

3.1. Update the Sparse Solution

At the p -th iteration, denotes the estimate of the phase compensation parameter $\alpha^{(p)}$. Accordingly, the filter function $H_{2(\alpha^{(p)})}$ and refocusing transform $\Gamma(s_{r_ROI})$ can be constructed according to Equations (10) and (11). The refocusing process described in (11) is reversible, and the inverse transform can be written as

$$s_{r_ROI} = \Gamma^{-1}(\Theta) = \mathbf{\Psi}_r^{-1} \cdot \left[(\mathbf{\Psi}_r \cdot \Theta \cdot \mathbf{\Psi}_a) \circ H_{2(\alpha)}^* \right] \cdot \mathbf{\Psi}_a^{-1}, \quad (12)$$

where $(\cdot)^*$ denotes the conjugate operation. Since the moving target is usually sparse in 2-D space domain, we can obtain the moving target imaging results by solving the following unconstrained problem [30,31]

$$\min_{\Theta} \|s_{r_ROI} - \Gamma^{-1}(\Theta)\|_2^2 + \lambda \|\Theta\|_1, \quad (13)$$

where $\|\cdot\|_1$ and $\|\cdot\|_2$ denote l_1 and l_2 norms, respectively, and $\lambda > 0$ is the regularization parameter that balances the recovery error and the sparsity of the solution. Given the value of $\alpha^{(p)}$, Equation (13) is a standard problem of sparse signal recovery. In this paper, we utilize the soft iterative thresholding algorithm [32] to solve Equation (13). The main steps are summarized below.

Soft Iterative Thresholding Algorithm

Input: s_{r_ROI} , λ , $\alpha^{(p)}$, $\Gamma(\cdot)$, and $\Gamma^{-1}(\cdot)$

Initialization: Let the iterative counter $k = 1$, residual matrix $R_0 = s_{r_ROI}$, and $\hat{\Theta}_0 = \mathbf{0}^{n_r \times n_a}$.

Iteration: at the k -th iteration ($k > 1$)

(1) Update the sparse result by $\hat{\Theta}_k = \text{soft}(\hat{\Theta}_{k-1} + \Gamma(R_{k-1}), \lambda)$, where $\text{soft}(x, \lambda) = \text{sign}(x) \cdot \max(|x| - \lambda, 0)$.

(2) Update the residual matrix by $R_k = s_{r_ROI} - \Gamma^{-1}(\hat{\Theta}_k)$.

(3) Increment k , and return to Step (1) until the stopping criterion is met. Here the stopping criterion is $\|\hat{\Theta}_k - \hat{\Theta}_{k-1}\|_2 / \|\hat{\Theta}_{k-1}\|_2 \leq \varepsilon$. The selection of the threshold value ε is related to the precision requirement.

Output: $\hat{\Theta}^{(p)} = \hat{\Theta}_k$.

3.2. Update the Estimate of Phase Compensation Parameter

Given the sparse solution $\hat{\Theta}^{(p)}$, the phase compensation parameter estimate can be updated by

$$\alpha^{(p+1)} = \alpha^{(p)} + \zeta \cdot \rho, \tag{14}$$

where ζ and ρ are iterative direction and iterative step-length, respectively. Further, the parameters $\{\zeta, \rho\}$ can be estimated by minimizing the recovery error, that is

$$\min \|s_{r_ROI} - \Gamma^{-1}(\hat{\Theta}^{(p)})\|_{F'} \tag{15}$$

where $\|\cdot\|_{F'}$ denotes F-norm of matrix. Substituting Equations (12) into (15), we have

$$\min \|\mathbf{Y} - \mathbf{U} \circ H_{2(\alpha)}^* \mathbf{\Psi}_a^{-1}\|_{F'} \tag{16}$$

where $\mathbf{Y} = \mathbf{\Psi}_r \cdot s_{r_ROI}$, and $\mathbf{U} = \mathbf{\Psi}_r \cdot \hat{\Theta}^{(p)} \cdot \mathbf{\Psi}_a$. Define $B_{(\alpha)} = \mathbf{U} \circ H_{2(\alpha)}^*$. According to (9) and (10), we have the expression of each element of $B_{(\alpha)}$ as

$$B_{(\alpha)}(\bar{f}_r, \bar{f}_a) = U(\bar{f}_r, \bar{f}_a) \cdot \exp\left\{-j\left[\frac{4\pi R_{ref}}{c} \sqrt{(f_c + \bar{f}_r)^2 + \frac{c^2 \bar{f}_a^2}{4} \left(\frac{1}{V^2} - \alpha\right)} - \frac{4\pi R_{ref}}{c} (f_c + \bar{f}_r)\right]\right\} \tag{17}$$

By taking the first-order Taylor expansion of $B_{(\alpha)}$, we have

$$B_{(\alpha)} = B_{(\alpha^{(p)})} + \left. \frac{dB_{(\alpha)}}{d\alpha} \right|_{\alpha=\alpha^{(p)}} \cdot \Delta\alpha \tag{18}$$

where $\Delta\alpha$ is the first-order increment. According to Equation (17), the derivative of $B_{(\alpha)}$ can be expressed as

$$\frac{dB_{(\alpha)}(\bar{f}_r, \bar{f}_a)}{d\alpha} = B_{(\alpha)}(\bar{f}_r, \bar{f}_a) \cdot \left(j \frac{\pi R_{ref} c \bar{f}_a^2}{2\sqrt{(f_c + \bar{f}_r)^2 + \frac{c^2 \bar{f}_a^2}{4} \left(\frac{1}{V^2} - \alpha\right)}} \right) \tag{19}$$

Then, Equation (16) can be rewritten as

$$\min \|\mathbf{Y} - B_{(\alpha^{(p)})} \cdot \mathbf{\Psi}_a^{-1} - \left. \frac{dB_{(\alpha)}}{d\alpha} \right|_{\alpha=\alpha^{(p)}} \cdot \mathbf{\Psi}_a^{-1} \cdot \Delta\alpha\|_{F'} \tag{20}$$

Define

$$\Xi^{(p)} = \left[\mathbf{Y} - B_{(\alpha^{(p)})} \cdot \mathbf{\Psi}_a^{-1} \right]_{Vector'} \tag{21a}$$

$$\mathbf{Z}^{(p)} = \left[\left. \frac{dB_{(\alpha)}}{d\alpha} \right|_{\alpha=\alpha^{(p)}} \cdot \mathbf{\Psi}_a^{-1} \right]_{Vector'} \tag{21b}$$

where $[\cdot]_{Vector}$ denotes the operation of stacking vectors one underneath the other sequentially, i.e., the size of $\Xi^{(p)}$ and $\mathbf{Z}^{(p)}$ are $n_r n_a \times 1$. Define

$$\mathbf{C}^{(p)} = \begin{bmatrix} \text{real}(\mathbf{Z}^{(p)}) \\ \text{imag}(\mathbf{Z}^{(p)}) \end{bmatrix}, \tag{22a}$$

$$\mathbf{D}^{(p)} = \begin{bmatrix} \text{real}(\Xi^{(p)}) \\ \text{imag}(\Xi^{(p)}) \end{bmatrix}, \tag{22b}$$

where $\text{real}(\cdot)$ and $\text{imag}(\cdot)$ denote the real and imaginary parts of a complex number, respectively. Then, the real-valued solution of the first-order increment can be directly obtained as

$$\Delta\alpha^{(p)} = \left([C^{(p)}]^T C^{(p)} \right)^{-1} [C^{(p)}]^T D^{(p)}, \quad (23)$$

where $[\cdot]^T$ denotes the transpose operation. Then the iterative direction and iterative step-length can be calculated as

$$\begin{cases} \zeta = \Delta\alpha / |\Delta\alpha| \\ \rho = \kappa \cdot |\Delta\alpha| \end{cases}, \quad (24)$$

where κ is the convergence parameter associated with the convergence speed, and it can be determined empirically. In the experiments of this paper, we set $\kappa = 10$. Finally, the phase compensation parameter can be updated by Equation (14).

By iteratively updating Θ and α as described above, the complete procedure of the parametric sparse representation method for moving target imaging is summarized in Figure 2. The iterative process is terminated until $|\alpha^{(p+1)} - \alpha^{(p)}| < \eta$, where η is the convergence threshold.

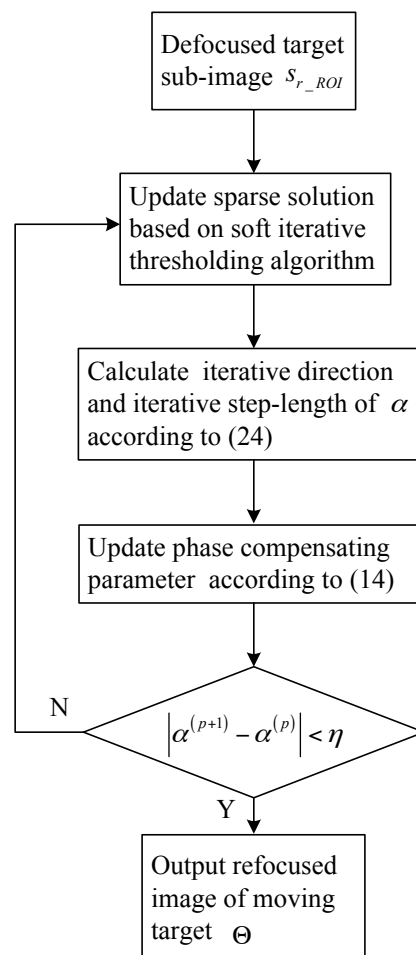


Figure 2. Flowchart of the parametric sparse representation method.

4. Experimental Results

The experimental results based on simulated data and real SAR data collected by GF-3 satellite are presented in this section to demonstrate the effectiveness of the proposed method.

4.1. Simulated Data

First of all, the proposed method is verified by using simulated data. The main system parameters are as follows. The carrier frequency is 10 GHz, the scene center range is 10 km, the platform velocity is 150 m/s, the transmitted bandwidth is 300 MHz, and the pulse duration is 2.2 μ s. The simulated scene contains 2 stationary reference scatterers (S1–S2) and a rigid-body moving target consisting of 4 scatterers (M1–M4), as shown in Figure 3. We first assume that the target only has constant-speed components in azimuth and range without acceleration. The actual velocity components of the target are set to be $v_x = 10$ m/s and $v_r = 5$ m/s. Figure 4 shows the imaging result obtained by the range migration algorithm (RMA) with the entire data, where the defocused sub-image containing the moving target, i.e., ROI, is indicated by the red dashed box.

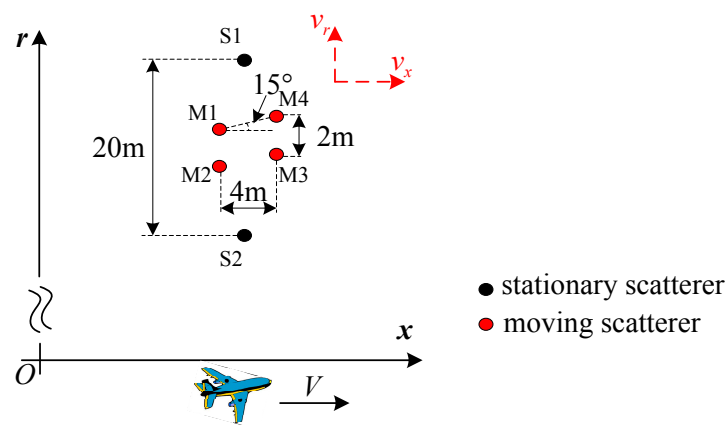


Figure 3. Simulation scene of a rigid-body moving target and two stationary reference points.

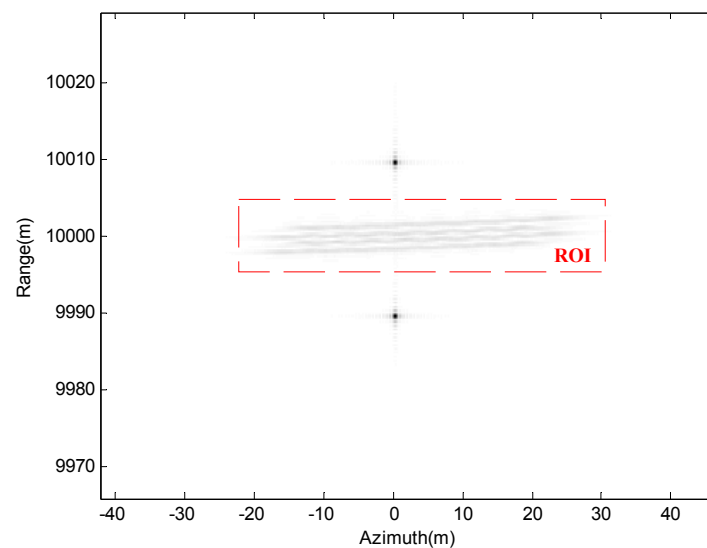


Figure 4. Range migration algorithm (RMA) imaging result with entire data.

By extracting the ROI sub-image from the regular SAR image, the data size is reduced to $n_r \times n_a$, i.e., 30×1051 . In the proposed method, the initialized value of phase compensation parameter is set as $\alpha^{(0)} = 1/150^2$. The convergence threshold in Figure 2 is set as $\eta = \alpha^{(0)}/10^4$. The convergence process of the phase compensation parameter estimation is shown in Figure 5. For comparison, the algorithm proposed in [16] is also employed in this experiment. The defocused ROI data and refocused results are shown in Figure 6. By 2-D searching, the method of [16] can accurately estimate the target

equivalent velocity. From Figure 6b,c, we can see that the image produces by the proposed method has a stronger contrast. The reason is that the sparse based method can effectively suppress the side-lobes.

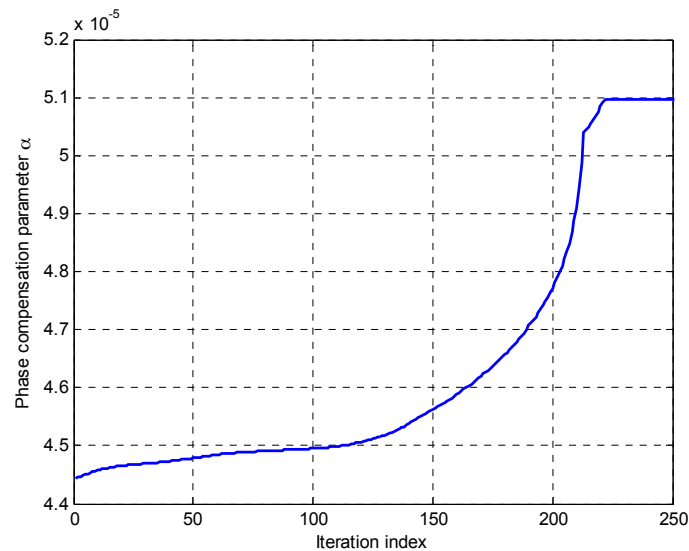


Figure 5. Convergence processes of the proposed method.

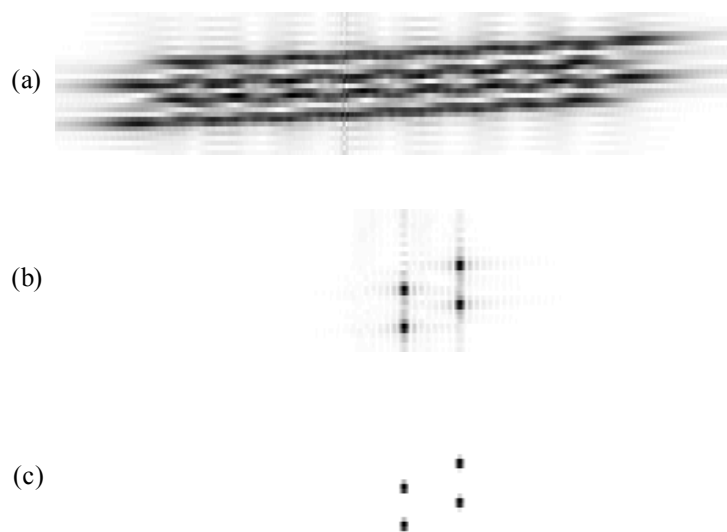


Figure 6. (a) Defocused region of interest (ROI) data; (b) refocused result obtained by the method in [16]; (c) refocused result obtained by the proposed method.

In the second simulation, the target in acceleration state is considered. The actual motion parameters of the point target are set to be $v_x = 10$ m/s, $v_r = 5$ m/s, azimuth acceleration $a_x = 1$ m/s², and range acceleration $a_r = 1$ m/s². By extracting the ROI sub-image from the regular SAR image, the data size is 41×2201 . The convergence process of the phase compensation parameter estimation is shown in Figure 7. The refocusing results obtained by the method in [16], and the proposed method are shown in Figure 8a,b, respectively. It is clear that the focusing performance of the method in [16] is seriously deteriorated. The reason is that this method cannot eliminate the high-order phase error caused by accelerative motion of the target. Moreover, we take the scatterer M3 on the target as example to analyze the refocusing quality. The range and azimuth profiles obtained by different methods are shown in Figures 9 and 10, respectively. One can find that the sub-image produced by the

proposed method can effectively suppress the asymmetric side-lobe and improve the image quality, which benefits from the superiority of the sparse constraint.

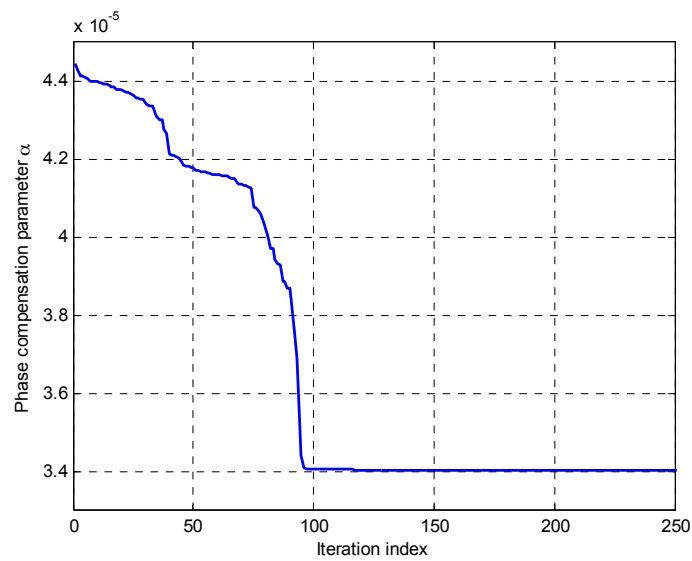


Figure 7. Convergence processes of the proposed method.

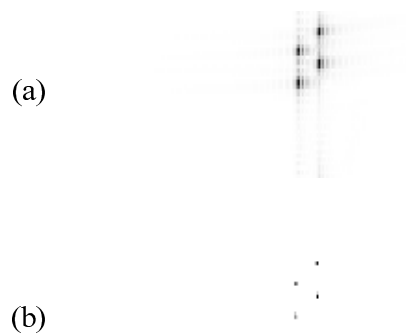


Figure 8. Refocusing result obtained by (a) method proposed in [16]; (b) the proposed method.

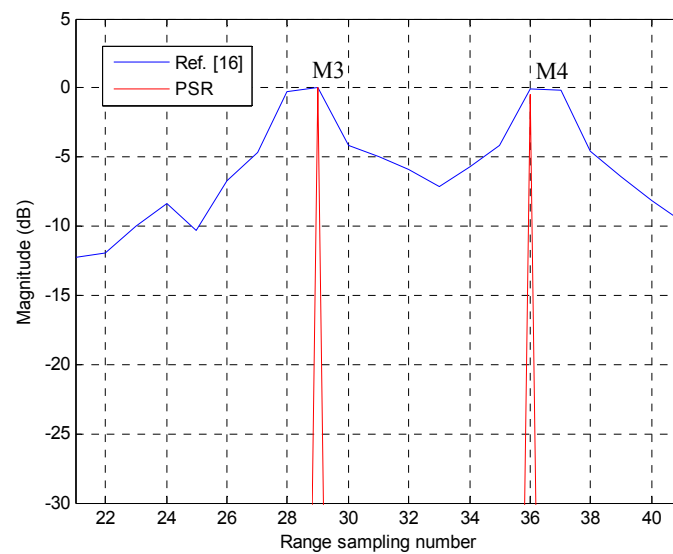


Figure 9. The range profiles of moving scatterer M3.

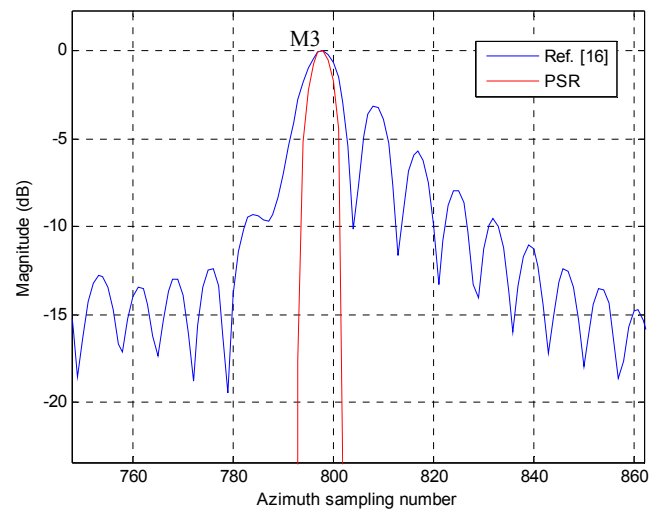


Figure 10. The azimuth profiles of moving scatterer M3.

4.2. Space-Borne Measured Data

We now present the experimental results by using the GF-3 space-borne SAR data containing moving ships. The regular SAR image of the sea surface is shown in Figure 11. We can see that the whole image is focused well, but some ships are defocused due to their movements. Three ROIs named T1, T2, and T3 containing moving ships are cropped from the original complex image, respectively. These three ships are processed sequentially using the method in [16] and the proposed method, respectively. Figure 12 shows the convergence processes of the phase compensation parameter of these moving ships. The refocused results obtained by the method in [16] and the proposed method are compared in Figures 13–15. It can be observed that the proposed method can successfully reconstruct images of moving ships and significantly suppress the side-lobes. To quantitatively compare different algorithms in terms of the image quality, the image entropy values of the refocused ROI images are listed in Table 1. The smaller value of image entropy means better focusing effect. As shown in Table 1, the proposed method can provide better image quality than the method in [16].

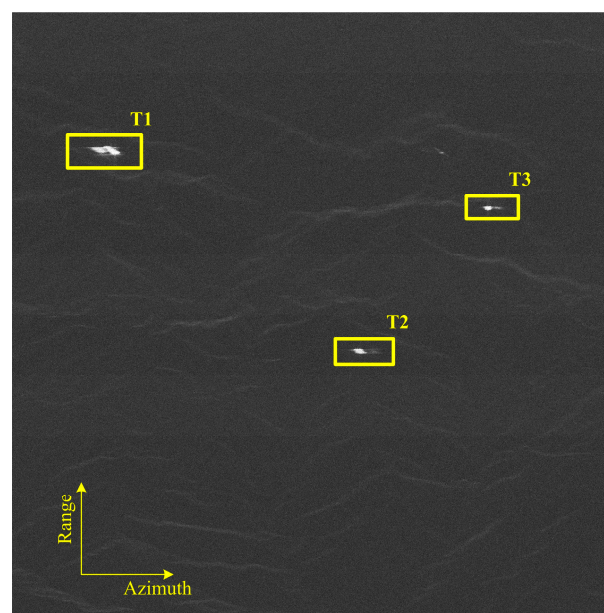


Figure 11. Regular imaging result of real data from GF-3 space-borne SAR.

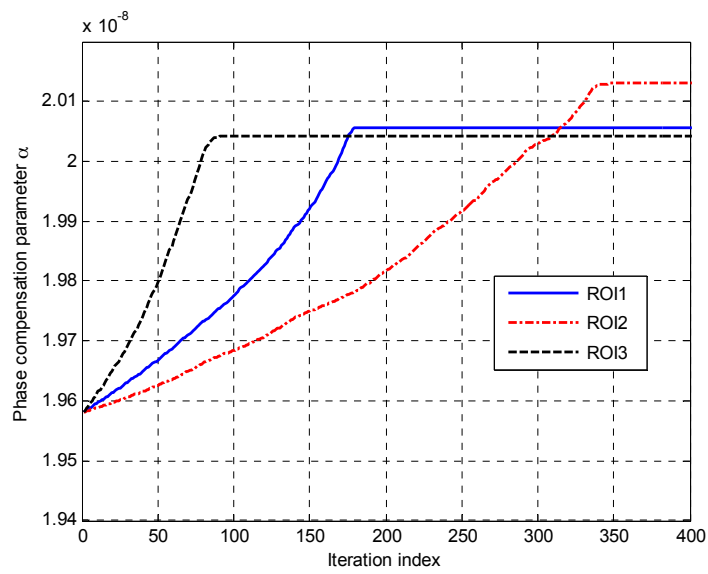


Figure 12. Convergence processes of the proposed method.

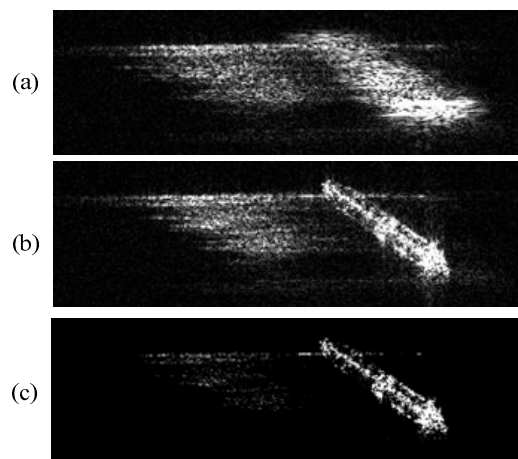


Figure 13. (a) Defocused ROI data of ship T1; (b) refocused result obtained by the method in [16]; (c) refocused result obtained by the proposed algorithm.

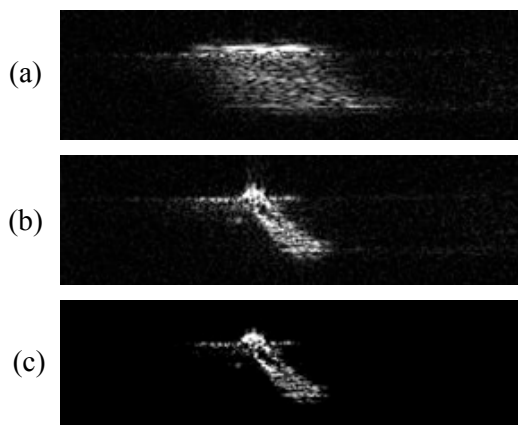


Figure 14. (a) Defocused ROI data of ship T2; (b) refocused result obtained by the method in [16]; (c) refocused result obtained by the proposed algorithm.

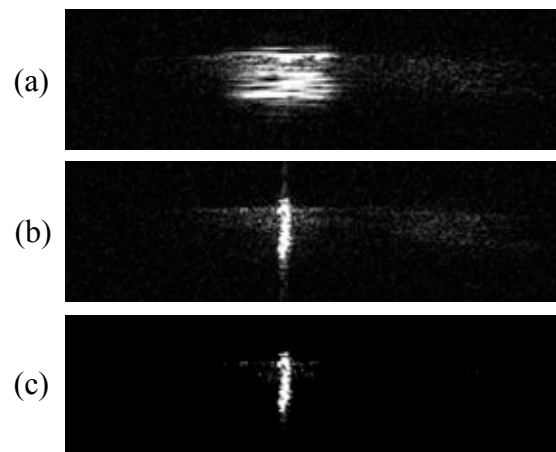


Figure 15. (a) Defocused ROI data of ship T3; (b) refocused result obtained by the method in [16]; (c) refocused result obtained by the proposed algorithm.

Table 1. The image entropy of the refocused ROI images.

| Targets and Methods | Ship T1 | | Ship T2 | | Ship T3 | |
|---------------------|-----------|--------|-----------|--------|-----------|--------|
| | Ref. [16] | PSR | Ref. [16] | PSR | Ref. [16] | PSR |
| Image Entropy | 6.4149 | 3.5389 | 6.3011 | 3.9863 | 5.077 | 4.0953 |

5. Conclusions

In this paper, we have presented a parametric sparse representation method for moving target imaging in SAR with ROI data. The ROI data extracted from regular SAR images is represented in a sparse fashion through a parametric refocusing transform. Then, the sparse image of the target and the phase compensation parameter are estimated by solving a joint the optimization problem through an iterative process. The proposed method works on the complex ROI data, rather than the raw entire data, which is helpful in reducing the amount of data and alleviating the clutter. Particularly, the proposed method can suppress asymmetric side-lobes and improve the image quality of moving targets, compared to the method in [16]. Experimental results based on both simulated and real space-borne SAR data validate the effectiveness of this method on refocusing the image of moving target using ROI data. Through our experiments, with the initial values as set in Section IV, we have never encountered the case where the proposed algorithm does not converge. A theoretical convergence analysis of the proposed algorithm will be studied in our future work.

Acknowledgments: This work was supported in part by the National Natural Science Foundation of China under Grants 61422110, 61631019, 61471019, and 61661130158, and in part by the National Ten Thousand Talent Program of China (Young Top-Notch Talent), and in part by the Tsinghua National Laboratory for Information Science (TNList), and in part by the Tsinghua University Initiative Scientific Research Program.

Author Contributions: All authors contributed extensively to the study presented in this manuscript. Gang Li proposed the methodology. Yichang Chen was responsible for data processing. Qun Zhang and Jinping Sun contributed to algorithm review, result discussion and manuscript review.

Conflicts of Interest: The authors declare no conflict of interest.

References

1. Werness, S.A.S.; Carrara, W.G.; Joyce, L.S.; Franczak, D.B. Moving target imaging algorithm for SAR data. *IEEE Trans. Aerosp. Electron. Syst.* **1990**, *26*, 57–67. [[CrossRef](#)]
2. Zhou, F.; Wu, R.; Xing, M.; Bao, Z. Approach for single channel SAR ground moving target imaging and motion parameter estimation. *IET Radar Sonar Navig.* **2007**, *1*, 59–66. [[CrossRef](#)]

3. Perry, R.P.; DiPietro, R.C.; Fante, R. SAR imaging of moving targets. *IEEE Trans. Aerosp. Electron. Syst.* **1999**, *35*, 188–200. [[CrossRef](#)]
4. Huang, P.; Liao, G.; Yang, Z.; Xia, X.G.; Ma, J.; Zheng, J. Ground maneuvering target imaging and high-order motion parameter estimation based on second-order keystone and generalized Hough-HAF transform. *IEEE Trans. Geosci. Remote Sens.* **2014**, *55*, 320–335. [[CrossRef](#)]
5. Gao, G.; Shi, G.; Yang, L.; Zhou, S. Moving target detection based on the spreading characteristics of SAR interferograms in the magnitude-phase plane. *Remote Sens.* **2015**, *7*, 1836–1854. [[CrossRef](#)]
6. Graziano, M.D.; D'Errico, M.; Rufino, G. Wake component detection in X-band SAR images for ship heading and velocity estimation. *Remote Sens.* **2016**, *8*, 498. [[CrossRef](#)]
7. Li, G.; Xia, X.G.; Xu, J.; Peng, Y.N. A velocity estimation algorithm of moving targets using single antenna SAR. *IEEE Trans. Aerosp. Electron. Syst.* **2009**, *45*, 1052–1062. [[CrossRef](#)]
8. Zhu, S.Q.; Liao, G.S.; Qu, Y.; Zhou, Z.G.; Liu, X.Y. Ground moving targets imaging algorithm for synthetic aperture radar. *IEEE Trans. Geosci. Remote Sens.* **2011**, *49*, 462–477. [[CrossRef](#)]
9. Zhu, D.Y.; Li, Y.; Zhu, Z.D. A keystone transform without interpolation for SAR ground moving-target imaging. *IEEE Geosci. Remote Sens. Lett.* **2007**, *4*, 18–22. [[CrossRef](#)]
10. Yang, J.G.; Huang, X.T.; Jin, T.; Thompson, J.; Zhou, Z.M. New approach for SAR imaging of ground moving targets based on a keystone transform. *IEEE Geosci. Remote Sens. Lett.* **2011**, *8*, 829–833. [[CrossRef](#)]
11. Sun, G.C.; Xing, M.D.; Xia, X.G.; Wu, Y.R.; Bao, Z. Robust ground moving-target imaging using deramp-keystone processing. *IEEE Trans. Geosci. Remote Sens.* **2013**, *51*, 966–982. [[CrossRef](#)]
12. Gu, F.F.; Zhang, Q.; Chen, Y.C.; Huo, W.J.; Ni, J.C. Parametric sparse representation method for motion parameter estimation of ground moving target. *IEEE Sens. J.* **2016**, *16*, 7646–7652. [[CrossRef](#)]
13. Wang, H.S.C. Mainlobe clutter cancellation by DPCA for space-based radars. In Proceedings of the IEEE Aerospace Applications Conference, Crested Butte, CO, USA, 3–8 February 1991.
14. Pascasio, V.; Schirinzi, G.; Farina, A. Moving target detection by along-track interferometry. In Proceedings of the International Geoscience Remote Sensing Symposium, Sydney, Australia, 9–13 July 2001.
15. Martorella, M.; Giusti, E.; Berizzi, F.; Bacci, A.; Dalle Mese, E. ISAR based technique for refocusing non-cooperative targets in SAR images. *IET Radar Sonar Navig.* **2012**, *6*, 332–340. [[CrossRef](#)]
16. Zhang, Y.; Sun, J.; Lei, P.; Li, G.; Hong, W. High-resolution SAR-based ground moving target imaging with defocused ROI data. *IEEE Trans. Geosci. Remote Sens.* **2016**, *54*, 1062–1073. [[CrossRef](#)]
17. Sjogren, T.K.; Vu, V.T.; Pettersson, M.I. Moving target refocusing algorithm for synthetic aperture radar images. In Proceedings of the IEEE International Geoscience Remote Sensing Symposium, Honolulu, HI, USA, 25–30 July 2010.
18. Onhon, N.O.; Cetin, M. SAR moving object imaging using sparsity imposing priors. *EURASIP J. Adv. Signal Process.* **2017**. [[CrossRef](#)]
19. Wu, Q.; Xing, M.; Qiu, C.; Liu, B.; Bao, Z.; Yeo, T.S. Motion parameter estimation in the SAR system with low PRF sampling. *IEEE Geosci. Remote Sens. Lett.* **2010**, *7*, 450–454. [[CrossRef](#)]
20. Khwaja, A.S.; Ma, J. Applications of compressed sensing for SAR moving-target velocity estimation and image compression. *IEEE Trans. Instrum. Meas.* **2011**, *60*, 2848–2860. [[CrossRef](#)]
21. Stojanovic, I.; Karl, W.C. Imaging of moving targets with multi-static SAR using an overcomplete dictionary. *IEEE J. Sel. Top. Signal Process.* **2011**, *4*, 164–176. [[CrossRef](#)]
22. Onhon, N.Ö.; Cetin, M. A sparsity-driven approach for joint SAR imaging and phase error correction. *IEEE Trans. Image Process.* **2012**, *21*, 2075–2088. [[CrossRef](#)] [[PubMed](#)]
23. Cetin, M.; Stojanovic, I.; Onhon, N.Ö.; Varshney, K.R.; Samadi, S.; Karl, W.C.; Willsky, A.S. Sparsity-driven synthetic aperture radar imaging: Reconstruction, autofocusing, moving targets, and compressed sensing. *IEEE Signal Process. Mag.* **2014**, *31*, 27–40. [[CrossRef](#)]
24. Zhao, L.F.; Wang, L.; Bi, G.A.; Yang, L. An autofocus technique for high-resolution inverse synthetic aperture radar imagery. *IEEE Trans. Geosci. Remote Sens.* **2014**, *52*, 6392–6403. [[CrossRef](#)]
25. Zhao, L.F.; Wang, L.; Yang, L.; Zoubir, A.M.; Bi, G. The race to improve radar imagery: An overview of recent progress in statistical sparsity-based techniques. *IEEE Signal Process. Mag.* **2016**, *33*, 85–102. [[CrossRef](#)]
26. Rao, W.; Li, G.; Wang, X.; Xia, X.-G. Parametric sparse representation method for ISAR imaging of rotating targets. *IEEE Trans. Aerosp. Electron. Syst.* **2014**, *50*, 910–919. [[CrossRef](#)]

27. Rao, W.; Li, G.; Wang, X.; Xia, X.-G. Adaptive sparse recovery by parametric weighted L1 minimization for ISAR imaging of uniformly rotating targets. *IEEE J. Sel. Top. Appl. Earth Obs. Remote Sens.* **2013**, *6*, 942–952. [[CrossRef](#)]
28. Li, G.; Zhang, H.; Wang, X.; Xia, X.-G. ISAR 2-D imaging of uniformly rotating targets via matching pursuit. *IEEE Trans. Aerosp. Electron. Syst.* **2012**, *48*, 1838–1846. [[CrossRef](#)]
29. Chen, Y.C.; Li, G.; Zhang, Q.; Zhang, Q.J.; Xia, X.G. Motion compensation for airborne SAR via parametric sparse representation. *IEEE Trans. Geosci. Remote Sens.* **2017**, *55*, 551–562. [[CrossRef](#)]
30. Donoho, D.L. Compressed sensing. *IEEE Trans. Inf. Theory* **2006**, *52*, 1289–1306. [[CrossRef](#)]
31. Candes, E.J.; Romberg, J.; Tao, T. Robust uncertainty principles: Exact signal reconstruction from highly incomplete frequency information. *IEEE Trans. Inf. Theory* **2006**, *52*, 489–509. [[CrossRef](#)]
32. Fang, J.; Xu, Z.; Zhang, B.; Hong, W.; Wu, Y. Fast compressed sensing SAR imaging based on approximated observation. *IEEE J. Sel. Top. Appl. Earth Obs. Remote Sens.* **2014**, *7*, 352–363. [[CrossRef](#)]



© 2017 by the authors. Licensee MDPI, Basel, Switzerland. This article is an open access article distributed under the terms and conditions of the Creative Commons Attribution (CC BY) license (<http://creativecommons.org/licenses/by/4.0/>).